

Modulation of delayed fluorescence pathways via rational molecular engineering

Received: 27 September 2023

Accepted: 7 February 2025

Published online: 26 March 2025

Check for updates

Sanchari Debnath ^{1,6}, Pria Ramkissoon ^{2,6}, Ulrike Salzner ³,
Christopher R. Hall ², Naitik A. Panjwani ⁴, Woojae Kim ⁵,
Trevor A. Smith ² & Satish Patil ¹ ✉

One of the key challenges in developing efficient organic light-emitting diodes (OLEDs) is overcoming the loss channel of triplet excitons. A common approach to mitigate these losses to enhance the external quantum efficiency of OLEDs is employing emitter molecules optimized for thermally activated delayed fluorescence (TADF) or triplet-triplet annihilation (TTA). However, achieving both in the solid state from the same organic chromophore poses a formidable challenge due to energetic and structural requirements needing to be met simultaneously. Here, we demonstrate TADF and TTA in donor-acceptor phthalimide derivatives by employing triphenylamine (TPA) or phenyl carbazole (PhCz) as a donor. Thin films of the TPA-substituted phthalimides doped in the poly(methyl methacrylate) matrix exhibit TADF emission from the singlet charge-transfer (CT) state. On the contrary, PhCz-substituted emitters display dominant TTA-induced delayed fluorescence in the neat film due to long-range molecular ordering that facilitates efficient triplet diffusion. The present study provides insight into how dual TADF-TTA delayed fluorescence can be realized in thin films of molecular semiconductors via rational molecular design.

Organic light-emitting diodes (OLEDs) have attracted immense attention in display and illumination technologies due to their flexible device structures and multicolor emission^{1,2}. OLEDs have several advantages over other display technologies, such as a brighter display with higher resolution and less power consumption than equivalent liquid crystal displays (LCDs)³. However, the primary impediments to large-scale OLED commercialization are limited lifetime, high cost, and poor efficiency. In a typical electroluminescence OLED device, uncorrelated charges are injected from electrodes, leading to a probability of singlet excitons (S_1) with 25% and triplet excitons (T_1) with 75% yield^{4,5}. Triplet excitons are long-lived with very low radiative efficiencies and are primarily unutilized, which limits the overall efficiency of OLEDs⁶. Over the years, OLED research has sought ways to overcome the inherent limitation imposed by charge recombination spin statistics.

A common approach uses organometallic complexes with ~100% phosphorescence efficiency from increased spin-orbit coupling^{7,8}. However, their high cost, limited photostability and possible toxicity limit the broad application of such OLEDs⁹. More recently, there has been a surge in the development of a new class of purely organic material that circumvents triplet exciton losses^{10–12}. In these materials, triplet excitons are harvested via thermally activated delayed fluorescence (TADF) and triplet-triplet annihilation (TTA). To trigger a rapid and efficient reverse intersystem crossing (rISC) in TADF molecules, a small S-T gap (ΔE_{ST}) stemming from an ultra-small exchange integral (J) is vital^{13–17}. Adachi and co-workers have demonstrated enhanced OLED device efficiency, with internal quantum efficiencies (IQE) up to 100%, by introducing purely organic TADF materials as emitters¹⁰. Although TADF has been extensively studied over the past decade, TTA is rarely

¹Solid State and Structural Chemistry Unit, Indian Institute of Science, Bengaluru, India. ²ARC Centre of Excellence in Exciton Science, School of Chemistry, University of Melbourne, Parkville, Australia. ³Department of Chemistry, Bilkent University, Ankara, Turkey. ⁴Berlin Joint EPR Lab, Fachbereich Physik, Freie Universität Berlin, Berlin, Germany. ⁵Department of Chemistry, Yonsei University, Seoul, Republic of Korea. ⁶These authors contributed equally: Sanchari Debnath, Pria Ramkissoon. ✉e-mail: spatil@iisc.ac.in

exploited because of its complicated mechanistic pathway. In the TTA process, two triplet excitons need to annihilate to generate an excited singlet state that emits delayed fluorescence (DF)¹⁸. As the annihilation of two triplets produces nine possible eigenstates, one singlet (¹TT), three triplets (³TT), and five quintets (⁵TT), the IQE of an OLED can be boosted up to a maximum of 62.5%¹⁸. In addition, TTA materials have potential applications in photovoltaics, photocatalytic devices, and biological imaging due to their ability to generate anti-Stokes emission via upconversion (TTA-UC)¹⁹. In TTA-UC, a series of energy-transfer steps involving a two-component system, usually an organometallic triplet sensitizer (or donor), and an annihilator (or acceptor) are required. Therefore, achieving the TTA process in an organic chromophore without the aid of a triplet sensitizer remains challenging. Furthermore, TTA is usually observed in solution, where the collision between triplets is feasible^{11,12}. In molecular films, however, TTA requires efficient triplet diffusion, which can be attained by increasing molecular concentration and tuning the molecular structure²⁰. Fused aromatic cores, e.g., anthracene, rubrene, pyrene, etc. display TTA upconverted delayed fluorescence. However, they require a sensitizer as they lack sufficient triplet population to facilitate annihilation. Therefore, a rational molecular design strategy for developing TTA-based delayed fluorescence emitters for OLEDs remains challenging²¹. Monkman and co-workers studied delayed fluorescence (DF) in exciplex systems by mixing different organic donor (D) and acceptor (A) materials²². They observed competing TADF and TTA emissions depending on the relative energy of the local triplet (³LE) state. Additionally, Zysman-Colman and co-workers reported heptacene-based emitters displaying dual TADF and TTA emission in which the TTA occurred after the TADF²³. However, TTA emission could only be achieved in a dilute THF solution, not a thin film²³. Conversely, they observed TADF emission in both solution and thin film. Therefore, controlling dual TADF and TTA-induced DF in the solid state from an organic molecule is difficult, and²⁴ demands unique molecular design criteria for its exploitation in OLEDs.

In the present work, we provide a molecular design strategy composed of a donor-acceptor system to exploit TTA and TADF. We have opted for an electron-deficient ‘phthalimide’, one of the smallest analogs of an aromatic imide, as the acceptor core^{25–28}. Although there are a few reports on phthalimide-based molecular systems as emitters in TADF-based OLEDs, an in-depth analysis of the photophysics of the delayed emission in those systems is seldom investigated^{29,30}. As electron donors, we have chosen electron-rich phenyl-carbazole

(PhCz) and triphenylamine (TPA) groups and substituted those to the phthalimide core to design two D-A and two D-A-D systems. The presence of carbonyl groups in the phthalimide core facilitates the intersystem crossing (ISC) rate through $n - \pi^*$ transitions in accordance with El-Sayed’s rule, which is a key requirement in TADF systems³¹. Though TPA and PhCz are structurally alike, the σ bond linking the two phenyl groups in PhCz yields a planar geometry compared to the twisted structure of TPA, which we envisage influences the excited state ‘charge transfer’ (CT) strength and enhances molecular ordering. We observed dominant TADF emission in the poly(methyl methacrylate) (PMMA) films of TPA-substituted phthalimide derivatives (1 wt.% doped). Conversely, DF originated from TTA dominated the neat films of PhCz-substituted phthalimide derivatives as a result of extended molecular packing via π -stacking facilitating efficient diffusion of triplet excitons. This study presents an effective approach to control delayed fluorescence through precise donor engineering.

Results and discussion

Synthesis

All four phthalimide derivatives were synthesized according to Fig. 1. Detailed synthetic schemes and procedures are given in the SI (Supplementary Note 1). The synthesis of mono-substituted phthalimide derivatives (Pth-1PCz and Pth-1TPA) was performed via Suzuki cross-coupling reaction using the boronic esters of phenyl carbazole (PhCz) and triphenylamine (TPA) (Fig. 1, Supplementary Fig. 1). The syntheses of the di-substituted phthalimide derivatives, i.e., Pth-2PCz and Pth-2TPA, were performed using the aforementioned donors and di-iodo-substituted phthalimide derivative via a similar Suzuki cross-coupling reaction (Fig. 1, Supplementary Fig. 2). All derivatives were well characterized using NMR spectroscopy and mass spectrometry, details of which are summarized in the SI (Supplementary Figs. 5–20).

Theoretical Calculations

Ground-state structures were optimized with the density functional theory (DFT) to gain insight into the relationship between molecular structures and electronic properties of phthalimide derivatives while varying the type and number of electron-donating groups. Energy-minimized structures for each of the mono- and di-substituted molecules are shown in Fig. 2a. These reveal major differences in the donor-acceptor dihedral angle; 37° for the mono-substituted derivatives Pth-1PCz and Pth-1TPA, whereas in the di-substituted derivatives, the dihedral angles between phthalimide and the donors increase to 49°

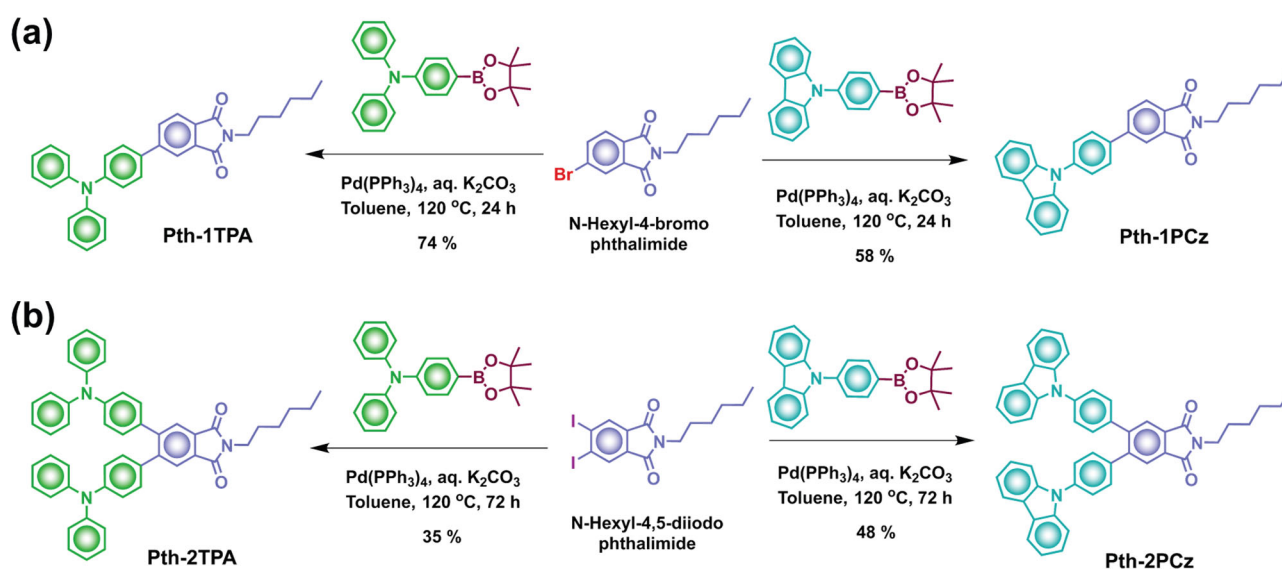


Fig. 1 | Molecular structures and synthetic route for the investigated molecules. Synthetic scheme of (a) mono and (b) di-substituted phthalimide derivatives.

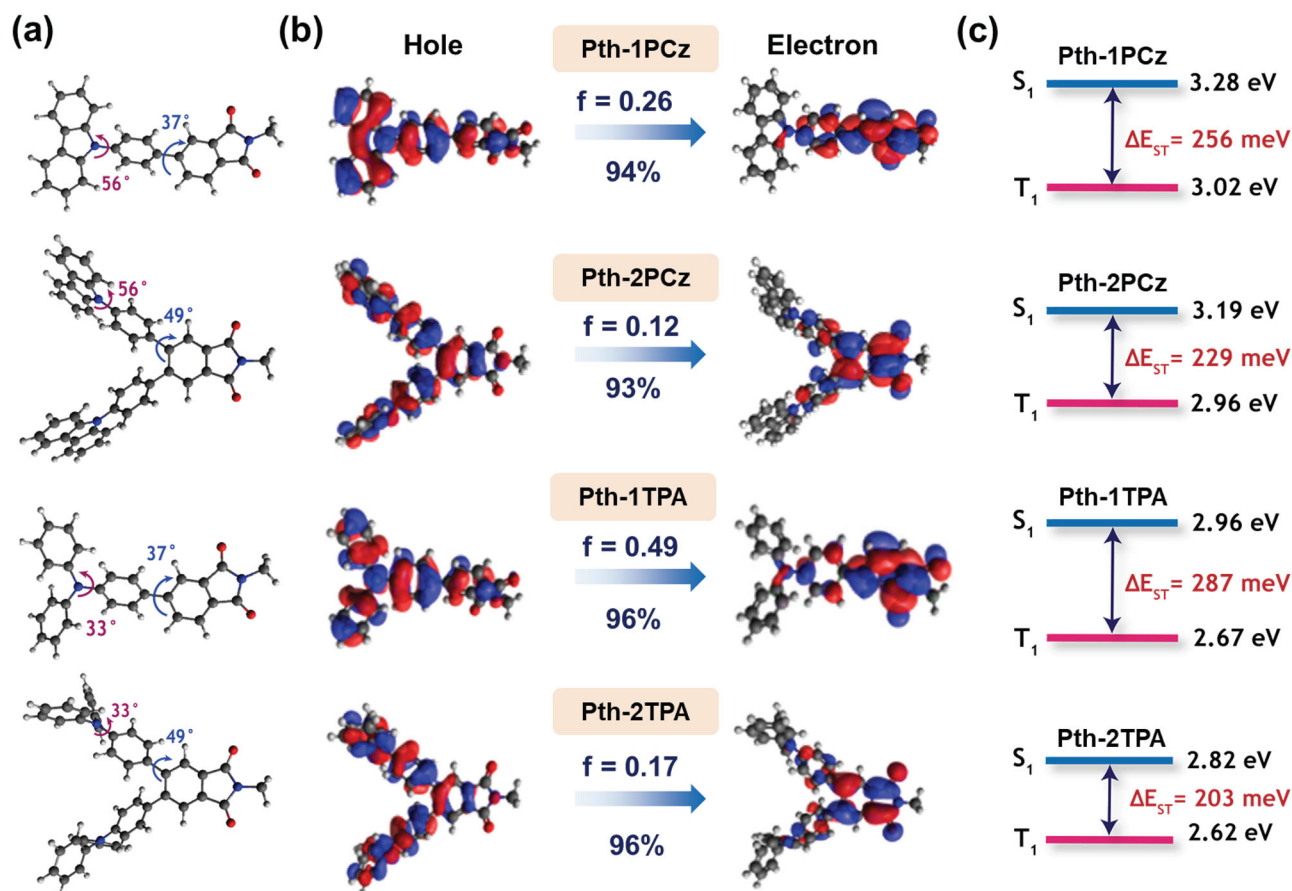


Fig. 2 | Theoretical calculation results of the investigated molecules.

a Calculated structures of Pth-1PCz, Pth-2PCz, Pth-1TPA and Pth-2TPA (from top to bottom) in the ground state (S_0) in chloroform. **b** Natural transition orbitals (NTOs) for the S_1 state at the optimized S_0 geometry for optical absorption in chloroform

(Hole and electron wave functions with the largest weight (%) and oscillator strengths (f) are provided), and **c** calculated vertical S_1 and T_1 energies and ΔE_{ST} of four phthalimide derivatives (in toluene). All the theoretical calculations were performed using the B3P86-30%/TVP-f level of theory.

for both PhCz and TPA (Fig. 2a), which can be ascribed to the steric hindrance between two *ortho*-linked donors. On the other hand, the dihedral angles between the carbazole and diphenylamine with the phenyl spacer are 56° and 33° , respectively (Fig. 2a). We also found that the rotational barriers of the mono- and di-substituted species are quite high (Supplementary Fig. 21), so it can be deduced that the lower energy minimum preference is over 99% in all cases at room temperature. From these differences in geometries, we expected two different perspectives regarding their electronic structures³². First, the larger dihedral angles in di-substituted derivatives would lead to smaller J values due to smaller overlaps between the hole and electron wavefunctions, giving rise to lower both ΔE_{ST} and oscillator strengths^{33,34}. Second, TPA, having stronger electron donating ability than PhCz owing to smaller dihedral angles between phenyl and nitrogen parts, reveals stronger conjugation so that both the S_1 and T_1 energy levels could be lowered. We confirm these speculations by calculating both the vertical (Franck-Condon point from S_0) and adiabatic (structurally relaxed) S_1 and T_1 energies (Fig. 2c and Supplementary Table 1) both in vacuum and when it may be affected by a dielectric medium. For Pth-1PCz and Pth-1TPA, adiabatic ΔE_{ST} values are less than or close to 300 meV, sufficient for the molecules to undergo TADF³⁵. For Pth-2PCz and Pth-2TPA, adiabatic ΔE_{ST} values are less than half the values of the singly substituted species, 0.13 and 0.12 eV in THF (Supplementary Table 1). The natural transition orbital (NTO) analysis further confirms that for the first singlet excited (S_1) state (Fig. 2b), hole and electron densities are primarily localized on the donor and acceptor part, respectively, supporting small ΔE_{ST} values for all chromophores. Spin orbit coupling matrix elements

(SOCME) between ground and the first two triplet states are small < 0.23 for Pth-1PCz and Pth-1TPA, and < 0.51 for Pth-2PCz and Pth-2TPA (Supplementary Tables 2–5). Pth-1PCz and Pth-1TPA couple more strongly between S_0 and T_1 , Pth-2PCz and Pth-2TPA couple mainly through S_0 and T_2 . The SOCME and ΔE_{ST} values indicate that rISC rates can be expected to be significantly larger for the doubly substituted than for the singly substituted species. However, the calculations do not predict any substantial difference between PhCz and TPA species. Since the electronic structures of these systems are very similar, one can safely assume that any DFT errors affect all the molecules similarly and that the lack of differences is not an artifact of DFT. The different photophysical properties of the PhCz and TPA species observed experimentally (see below) must therefore be caused by effects beyond electronic structure differences.

Photophysics in solution

The photophysical properties of the phthalimide derivatives were determined with steady-state UV-visible absorption and emission measurements in a dilute solution (Fig. 3a). In Pth-1PCz and Pth-2PCz, we observe sharp absorption bands in the 280–360 nm region, which are assigned to π - π^* transitions as local excitations (LE) on the carbazole donor group (Fig. 3a, Supplementary Fig. 22a, b). The broad feature at lower energy (360–440 nm) exhibits a red shift with an increase in the solvent polarity (from non-polar cyclohexane to polar chloroform), indicating its charge-transfer (CT) nature from the interaction between the electron-rich carbazole and the electron-deficient phthalimide moiety (Supplementary Fig. 22a, b). Similar ‘CT’ features are also observed in Pth-1TPA and Pth-2TPA (Fig. 3a,

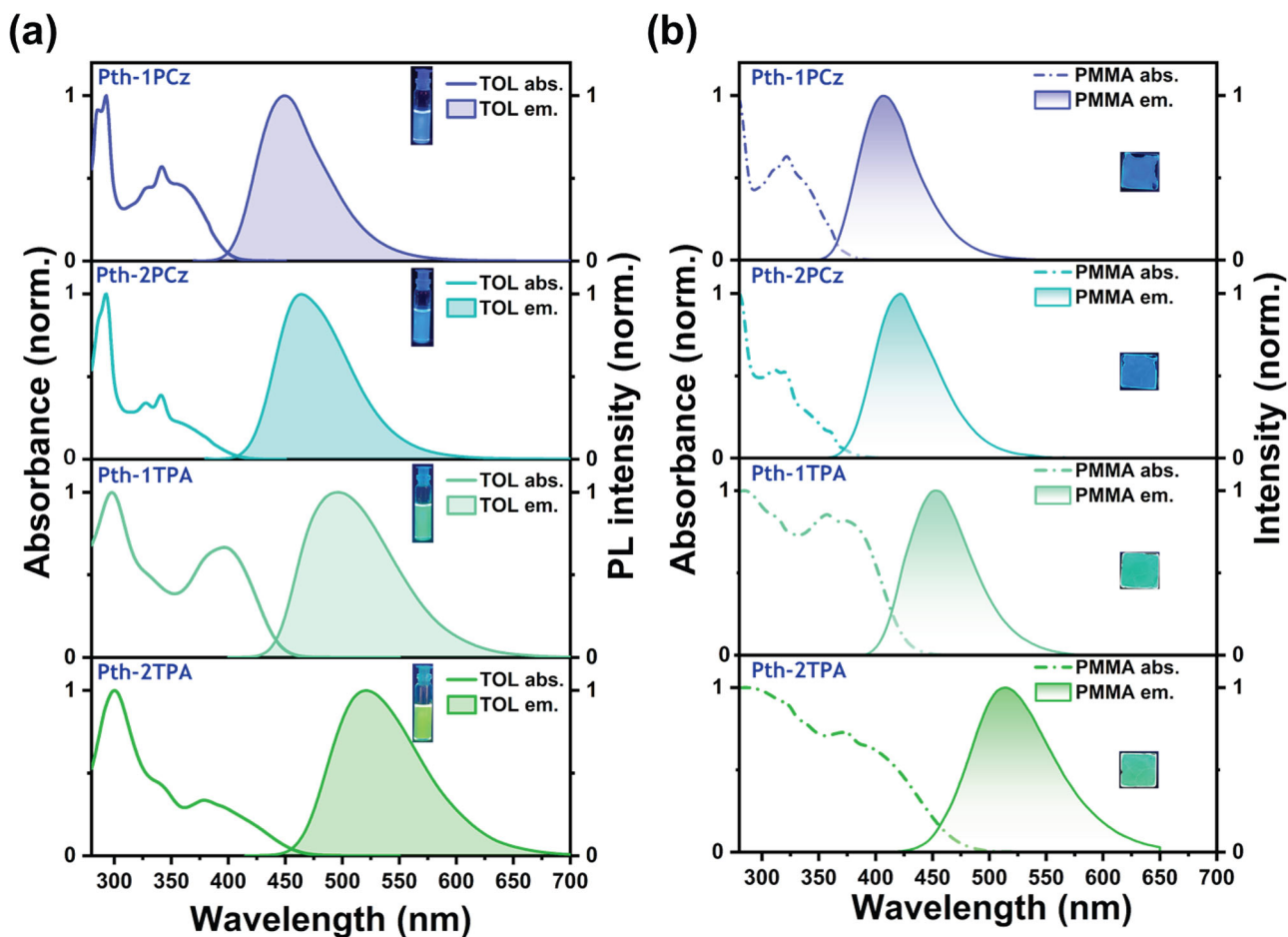


Fig. 3 | Absorption and emission spectra of the investigated molecules in solution and thin film. Normalized UV-visible absorption and emission spectra for the four phthalimide derivatives in (a) dilute toluene solution and (b) 1 wt.% doped in PMMA matrix ($[c] = 10 \mu\text{M}$ for all solution measurements, $\lambda_{\text{exc.}} = 360, 370, 390,$

and 405 nm for Pth-1PCz, Pth-2PCz, Pth-1TPA and Pth-2TPA, respectively, for both solution and PMMA film; the inset photographs were taken under UV light excitation).

Supplementary Fig. 22c, d). The corresponding emission spectra are broad and structure-less for all the derivatives and show strong solvatochromism as bathochromic shifts in solvents of increased polarities, consistent with the formation of a CT state (Fig. 3a, Supplementary Figs. 23–24)^{28,36}. Time-resolved emission measurements in dilute toluene solution give CT lifetimes of 4.79, 8.38, 5.08, and 9.47 ns for Pth-1PCz, Pth-2PCz, Pth-1TPA, and Pth-2TPA, respectively, consistent with differences in transition oscillator strength calculated for each derivative (Supplementary Fig. 25). All other photophysical data are summarized in Supplementary Tables 6–9.

Photophysics in the solid state

Steady state photophysical studies of the four derivatives in thin films were performed to understand the behavior of the molecules in the solid state, as it is more relevant to OLED fabrication. To prevent aggregation and effectively harvest the triplet excitons, we dispersed a small amount of the molecule (1 wt.%) in a polymeric host poly(methyl methacrylate) (PMMA), which is well-known to reduce triplet exciton quenching by minimizing vibrational dissipation and oxygen permeability³⁷. The steady-state absorption and emission spectra of the derivatives in the PMMA matrix are shown in Fig. 3b. All the phthalimide derivatives exhibit intense emission in PMMA film with high PLQYs of 92, 84, 95, and 74% in Pth-1PCz, Pth-2PCz, Pth-1TPA, and Pth-2TPA, respectively (Supplementary Table 10). These values are reminiscent of the PLQYs measured in low-polarity solvents (Supplementary Tables 6–9). The prompt fluorescence (PF) lifetimes of the

derivatives measured by TCSPC are 5.89, 9.96, 6, and 11.47 ns for Pth-1PCz, Pth-2PCz, Pth-1TPA, and Pth-2TPA, respectively (Supplementary Fig. 26, Supplementary Table 10), comparable to the dilute low-polar solvents.

To obtain a deeper understanding of the photophysical phenomena occurring in the polymeric matrix, we conducted time-resolved gated emission measurements at both room temperature (RT) and 77 K to capture the full emission evolution from prompt to delayed fluorescence to phosphorescence (PH) (Figs. 4a, 5a, Supplementary Figs. 27a, 28a). When TADF occurs, the intensity of the delayed component increases with increasing temperature, indicating that thermal energy activates the delayed emission³⁸. Conversely, an inverse temperature dependence is found for PH³⁸. Here, we record data spanning over eight orders of magnitude in time and twelve orders in intensity, revealing decay kinetics with PF and two regions of DF (Figs. 4b, 5b, Supplementary Figs. 27b, 28b). In the millisecond time range, the films also show PH at 77 K and RT in an oxygen-free environment (Supplementary Fig. 29). We observe a significant enhancement in phosphorescence intensity under oxygen-free conditions compared to ambient conditions, likely due to decreased quenching of triplet excitons by oxygen in air³⁹. Fig. 4a shows PF, DF (at 100 μs delay) and the PH spectra (1 ms delay) for Pth-2TPA. Interestingly, two distinct DF regions are observed in the time-resolved emission profiles for Pth-2TPA (Fig. 4b). The first DF region (~ 200 ns to 7 μs) displays no prominent temperature dependence. Conversely, the second DF region (20 μs to 900 μs) shows significant intensity enhancement upon

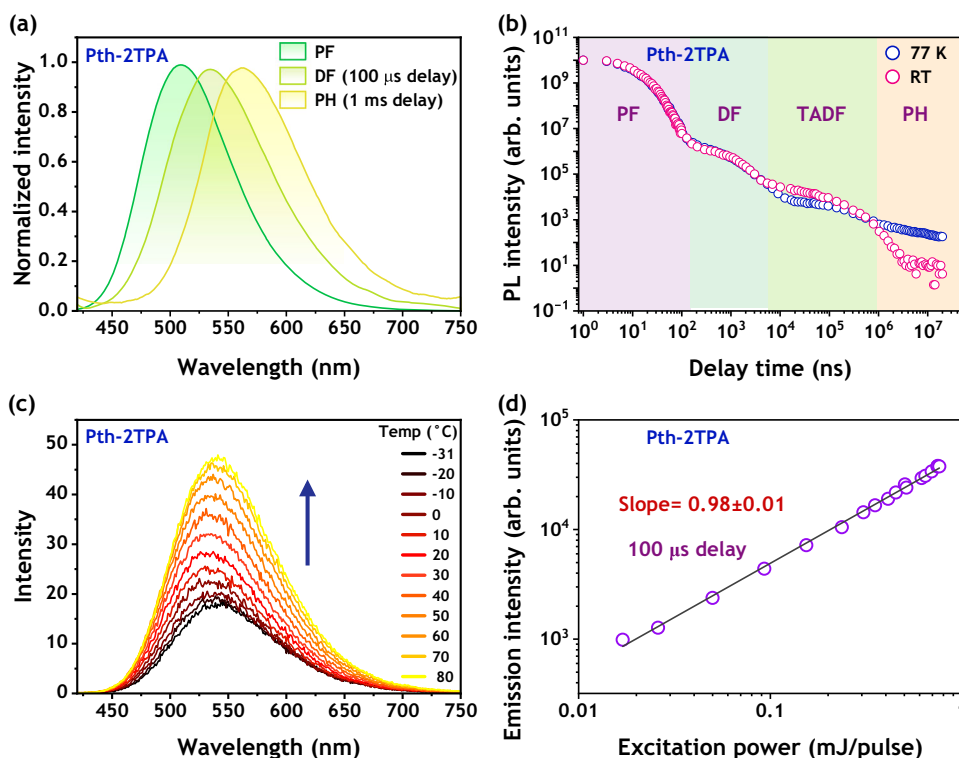


Fig. 4 | Evidence of thermally activated delayed fluorescence (TADF) in thin film of Pth-2TPA. **a** Plots of normalized PF (prompt fluorescence), DF (delayed fluorescence at 100 μ s delay) at room temperature and PH (phosphorescence at 1 ms delay) at 77 K for Pth-2TPA. **b** Decay kinetics of 1 wt.% Pth-2TPA in PMMA film as a

function of delay time at RT and 77 K, respectively. **c** Temperature-dependent study of Pth-2TPA (1 wt.% in PMMA matrix) emission at 100 μ s delay ($\lambda_{exc.} = 400$ nm). **d** Emission intensity as a function of laser excitation energy at 100 μ s delay, 500 μ s gate for 1 wt.% Pth-2TPA in PMMA film.

temperature increase from 77 K to RT. A systematic temperature-dependent study of Pth-2TPA at 100 μ s delay (Fig. 4c) shows a monotonic increase with temperature, indicative of thermal activation of the second DF region. The DF could result from either TADF or TTA processes, which can be identified from their excitation power dependence; TADF shows a linear dependence on the emission intensity, whereas TTA shows quadratic dependence⁴⁰. For Pth-2TPA, the power dependence (Fig. 4d, Supplementary Fig. 30a) for the first and second DF regions (Time Delay/TD = 1 μ s and 100 μ s) yield slopes of 1.26 and 0.98, respectively. This suggests that TADF is the dominant DF mechanism in the second DF region, whereas, in the first DF region, a value slightly higher than unity implies the possibility of a negligible contribution to the TTA process. Furthermore, the TADF dynamics in Pth-2TPA are consistent with the observations in similar TADF systems^{15,41}, in that the kinetics of the entire decay can be modeled with a sequence of decay laws, concordant with the dominant monomolecular processes observed (Supplementary Fig. 31a). The lowest energy onset of the PF spectrum provides the S_1 energy of 2.02 eV above the ground state (Supplementary Table 11). The T_1 energy obtained from the lower energy onset of the phosphorescence spectrum is estimated as 1.84 eV above the ground state (Supplementary Table 11). The corresponding ΔE_{ST} of 180 meV is sufficient to facilitate rISC observed in Pth-2TPA. All the kinetic parameters are summarized in Supplementary Table 12.

Markedly different behavior is observed for Pth-1TPA (Supplementary Fig. 27a, b). The first DF region shows a slope of 1.51 (when TD = 1 μ s) (Supplementary Fig. 30b). Slopes with intermediate values between 1 and 2 have been observed previously²². This is usually interpreted as being due to both TTA and TADF processes operating within a given time regime (such as DF region 1), and with TTA being a bimolecular process and therefore slow, it competes with the rISC process²². The second DF region, however, displays a lower slope of

1.03. Since the energy gap between the S_1 and T_1 excited states is moderate (~ 250 meV), rISC can occur, facilitating TADF emission (Supplementary Table 11), and the slope near unity identifies the origin of the second DF region as a TADF process (Supplementary Fig. 27c). In this case, a fitting analysis of the Pth-1TPA decay kinetics (Supplementary Fig. 31b) shows it can be modeled using an exponential decay law for the PF region (< 50 ns) and a power law (t^n) evolution after ~ 50 ns for TTA recombination characteristic of triplet diffusion. Specifically, two power law slopes (-0.68 and -1.55) are extracted between 50 ns and 20 μ s, indicative of a transition from dispersive triplet diffusion in nonequilibrium to a nondispersive regime where triplet diffusion is in equilibrium⁴². This behavior confirms the presence of TTA in these systems and is consistent with what has been observed in the decay curves of other films for similar applications²³. Therefore, the Pth-1TPA system can exhibit both TADF and TTA under specific conditions. Overall, Pth-1TPA displays both TTA-DF and TADF emission, whereas in Pth-2TPA, due to relatively smaller ΔE_{ST} , rISC-mediated TADF appears to be the dominant pathway.

To understand the effect of donor strength and geometry on the photophysics of phthalimide-based emitters, we also performed the same experiments for PhCz- substituted derivatives (Fig. 5, Supplementary Fig. 28). We envisaged that a change in donor strength from TPA to PhCz would tune the rISC mechanism and subsequently yield different DF characteristics. The change yielded a switch in the dominant mechanism for DF, as shown by the temperature-dependent emission kinetics in Fig. 5b, Supplementary Fig. 28b. For Pth-1PCz, a quadratic dependence on the excitation dose was observed with a slope of 1.89 (at TD = 100 μ s) and 1.61 (at TD = 1 μ s) (Fig. 5c, Supplementary Fig. 32), suggesting TTA dominated DF in all delay regions. A similar quadratic dependence was observed for Pth-2PCz (Supplementary Fig. S28c). The dominant TTA behavior was further confirmed by the power law slopes that were fit to the decay curves

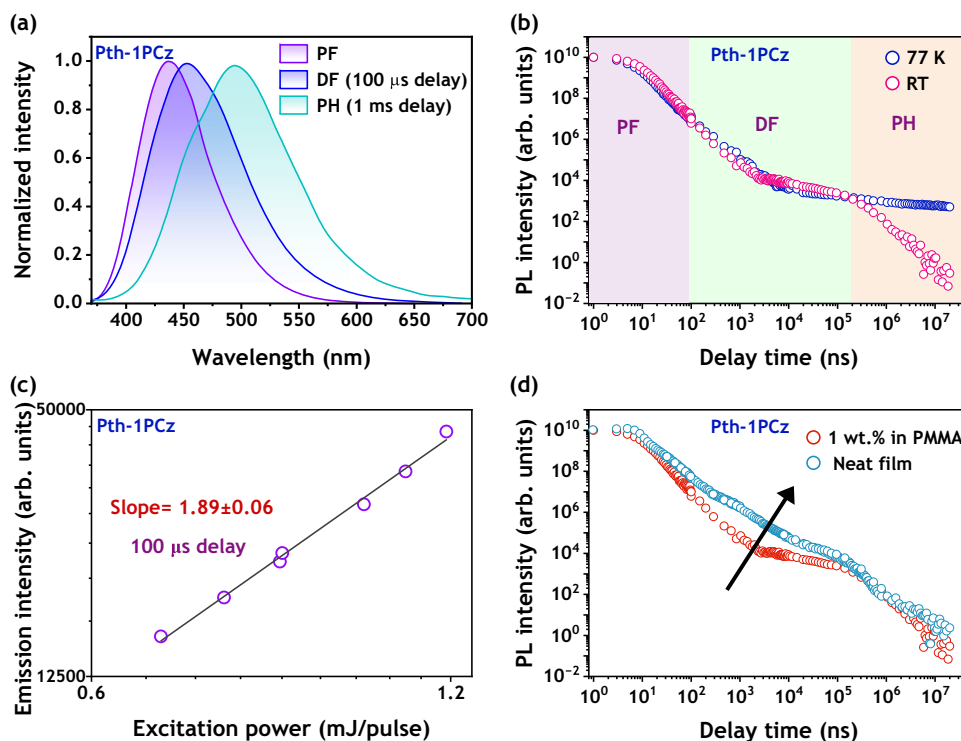


Fig. 5 | Signature of delayed fluorescence via triplet-triplet annihilation (TTA) in thin film of Pth-1PCz. (a) Plots of normalized PF (prompt fluorescence), DF (delayed fluorescence at 100 μ s delay) at room temperature and PH (phosphorescence at 1 ms delay) at 77 K. (b) Decay kinetics of 1 wt.% Pth-1PCz PMMA film as a

function of delay time at RT and 77 K, respectively. (c) Emission intensity as a function of laser excitation power at 100 μ s delay, 150 μ s gate for Pth-1PCz. (d) Comparison in decay kinetics of Pth-1PCz in 1 wt.% PMMA vs. neat film.

(Supplementary Fig. 33a, b). Both Pth-1PCz and Pth-2PCz show a similar and characteristic evolution from a dispersive to a nondispersive triplet diffusion regime after ~ 1 μ s with power law slopes close to -0.5 and -2 , respectively. Pth-1PCz also shows nondispersive triplet diffusion (slope -2.63) after the PF, consistent with nearly pure TTA in the 100 μ s time regime. As the experimentally calculated ΔE_{ST} for these systems is relatively large: 290 and 340 meV for Pth-1PCz and Pth-2PCz, respectively (Supplementary Table 11), we anticipate that TTA outcompetes the rISC process and becomes the dominant DF pathway. Therefore, the PhCz-substituted derivatives seem to exhibit TTA-induced DF exclusively. While there are several reports of TTA-induced DF in the solution state, in the thin film it is rarely observed, with most examples being in polymeric films^{43–45}. Highly efficient TTA in molecular films requires efficient triplet diffusion, which can be increased by increasing molecular ordering²⁰. Two conditions necessary for the TTA process are: i) an efficient ISC rate to generate the triplet state and ii) a long triplet diffusion length with efficient triplet migration. A high ISC rate can be optimized through a molecular configuration designed to increase the spin-orbit coupling (SOC)³¹. We speculate that in phthalimide chromophores presented in this work, the presence of two C=O groups allows access to the triplet manifold through $n - \pi^*$ transitions, resulting in sufficient ISC to generate a large number of triplet excitons⁴⁶. Long-range molecular ordering is also required for efficient triplet diffusion, which can be achieved by $\pi - \pi$ stacking in the molecular arrangement^{45,47}. From our studies in PMMA films doped with PhCz-based phthalimides, we observed a contribution of TTA in the DF, hinting towards triplet exciton migration even in the dispersed conditions (Fig. 5a–c, Supplementary Figs. 28, 32). Therefore, in principle, annihilation of triplets should be enhanced with increased molecular concentration. To validate this assumption, we carried out time-resolved emission studies for the neat films of PhCz-based systems. The decay curves for neat films of Pth-1PCz and Pth-2PCz show significant enhancement in the DF intensity (Fig. 5d, Supplementary

Fig. 35a) relative to their 1 wt.% in PMMA films. Further, the excitation power-dependent studies display characteristic power law slopes in the decays, and slopes change from -2 to -1 (saturation) in the power dependence plot (Supplementary Figs. 34, 35b). This observation provides evidence for enhanced TTA propensity in neat films of PhCz-based phthalimide derivatives.

To further validate our observation of TTA-dominant DF in PhCz-based systems, we utilized optically detected magnetic resonance (ODMR) as a characterization technique. ODMR can be used to study systems where resonant microwave irradiation leads to changes in the corresponding photoluminescence intensity. As TTA is a spin-dependent process, resonant microwave irradiation with the triplet transitions should lead to changes in the corresponding DF intensity. Hence, to study the process of TTA in both Pth-1PCz and Pth-2PCz, we employed photoluminescence-detected magnetic resonance (PLDMR).

Shown in Fig. 6 is the PLDMR of Pth-2PCz neat film measured at 80 K, with continuous 365 nm excitation. We first measured the PLDMR spectra by collecting all PL above 400 nm; in this case, we collected PL due to PF, DF, and PH from the sample. Under these conditions, we observed strong signals corresponding to $|\Delta m_s| = 1$ (full-field) and $|\Delta m_s| = 2$ (half-field) transitions. Similarly, full- and half-field transitions were observed in the PLDMR of Pth-1PCz (Figure S16). The detection of $|\Delta m_s| = 2$ (half-field) transitions, along with simulations of the full- and half-field features confirms the detection of photoexcited triplet states. We then measured the same samples under the same conditions, with two different wavelength detection windows of 400–550 nm and 400–450 nm (see Fig. 6 and Supplementary Fig. 36). In each case, we saw the same PLDMR triplet signals present. As we reduced the wavelength detection window, the PLDMR spectra became more dominated by changes in the fluorescence intensity. Since PF is a spin-independent process and DF due to processes such as TTA is a spin-dependent process, the observed PLDMR

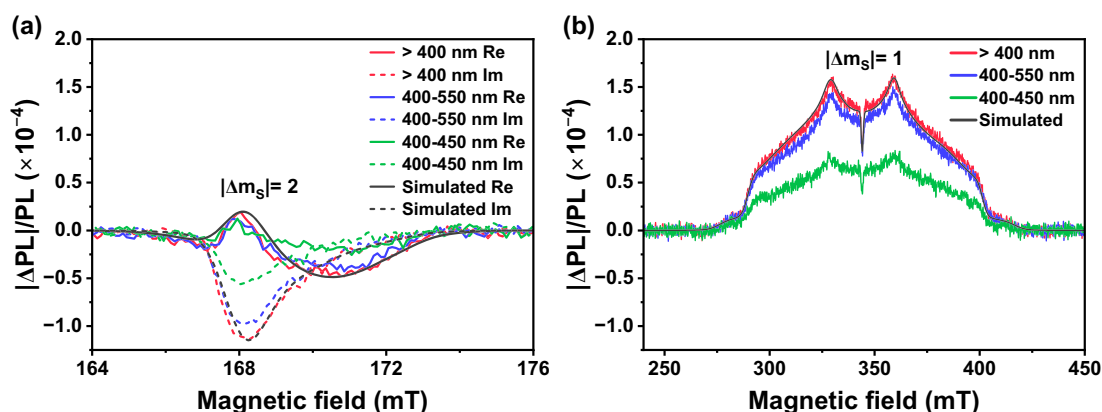


Fig. 6 | PLDMR spectra of Pth-2PCz in neat film. PLDMR of Pth-2PCz neat film measured at 80 K under 365 nm excitation at three different detection windows of > 400 nm (red line), 400-550 nm (blue line), and 450-450 nm (green line), and the corresponding simulations (black line). **a** The half-field spectrum (solid and dashed

lines showing experimental data observed in the real (Re) and imaginary (Im) channel of the lock-in, respectively), **b** showing the full-field spectrum (only showing real channel as a negligible signal is in the imaginary channel).

response (particularly in the 400-450 nm PLDMR) must be due to DF in these samples. In combination with the observed quadratic dependence of DF intensity vs excitation energy in the optical studies (Fig. 5c and Supplementary Fig. 28c), the PLDMR on Pth-IPCz and Pth-2PCz strongly indicates TTA is active in these materials even at 80 K. Having carried out PL experiments monitoring the DF emission intensity as a function of excitation energy, we see that both Pth-IPCz and Pth-2PCz in neat films exhibit at low excitation energies a slope of -2 while at higher excitation energies a slope of -1 (Supplementary Figs. 34–35), which is consistent with a TTA process. The PLDMR experiments were carried out on neat films. Note, that the same material when in a dilute 1 wt.% concentration in PMMA, exhibits a slope of -2 throughout the measured excitation energy range, as expected for a TTA process. Hence, we conclude that the PLDMR response must be due to DF coming from a TTA process.

To further support our hypothesis, we have analyzed the crystal structure of both Pth-IPCz and Pth-2PCz. Pth-IPCz forms a triclinic crystal system with a space group of $P\bar{1}$ and $Z=2$ (Fig. 7a, Supplementary Fig. 37). Intramolecular H-bonds are present in the molecule at distances of 2.619 and 2.644 Å between the phthalimide oxygens and the H- atoms of the C-1 of the hexyl chain (Fig. 6b). Pth-IPCz units exhibit inter-molecular C-H...O interactions at a distance of 2.381 Å, which also offers additional ordering in the molecular structure (Fig. 7b). Two Pth-IPCz molecules are stacked together by a $\pi-\pi$ distance of 3.232 Å, as shown in Fig. 7c. In the Pth-IPCz crystal, the individual units are stacked with alternating $\pi-\pi$ distances of 3.367 and 3.378 Å, respectively, providing a long-range molecular ordering depicted in (Fig. 7d), which may facilitate triplet migration. On the other hand, in Pth-2PCz, the molecules are held together with C-H...O interactions (2.671 Å) between C=O of the phthalimide with phenyl hydrogens of the spacer ring through the hydrogen bonding network resulting in the formation of the molecular dimer⁴⁸. The molecule is held together by the C-H... π interactions through separations of 2.854, 2.868, and 2.896 Å (Supplementary Fig. 38). In addition to C-H...O and C-H... π interactions, Pth-2PCz also exhibits $\pi-\pi$ interactions over 3.385 Å indicative of strong $\pi-\pi$ overlap in the molecular ensemble (Supplementary Fig. 38). From the in-depth crystal structure analysis, we anticipate that the Cz-substituted derivatives show long-range molecular ordering via strong $\pi-\pi$ interactions (Supplementary Figs. 39–40), which enhances the triplet diffusion propensity in the solid state, thereby facilitating the TTA process. These results show that solid-state packing in PhCz-based phthalimide systems plays a significant role in the TTA-induced DF process, providing direction

towards the design of efficient TTA-based DF emitters. We expect that further analyzing the electroluminescence of the four compounds might provide a clear understanding of the differences between TTA and TADF materials, offering valuable insights for future OLED applications, which could serve as an extension of the current work.

To investigate the mechanistic pathway, we collected the phosphorescence spectra for the neat donors (PhCz and TPA) and the acceptor (Pth-Hex) as 1 wt.% PMMA films (at 77 K with 1 ms delay time) and compared those with the phosphorescence spectra of the four derivatives (Supplementary Fig. 41). From the onset of the phosphorescence spectra, we estimated the triplet energies of the neat D/A units, which have been calculated to be 2.33, 2.52 and 2.28 eV for PhCz, TPA and Pth-Hex, respectively (Supplementary Table 13). Interestingly, the phosphorescence spectra of all four phthalimide derivatives appear to possess CT character because of their broad and structureless profiles and are at lower energies than the phosphorescence spectra of the individual D (PhCz and TPA) and A (Pth-Hex) units (${}^3LE_{D/A}$). This result indicates that the lowest energy triplet state of these phthalimide derivatives is CT (3CT) in nature, which is vibronically coupled with the ${}^3LE_{D/A}$ state. We also envisage that due to the large energy difference between the 3CT and the ${}^3LE_{D/A}$, the latter do not participate in the rISC; instead, the lowest energy triplets of the molecule participate in the rISC process. Thus, we propose that in TPA-based systems, the molecules undergo rISC mediated from a 3CT state (Fig. 8). On the contrary, although many triplets (3CT) are generated in PhCz-based systems, due to increased long-range molecular ordering, TTA surpasses rISC and generates delayed fluorescence (Fig. 8).

In summary, we have designed four phthalimide-based D-A chromophores using two structurally different donors to convert dark triplet states into emissive states. TPA-based phthalimide emitters dispersed in PMMA films display a predominant thermally activated DF process owing to small ΔE_{ST} . PhCz-based emitters, on the contrary, provide a signature of TTA-induced DF in PMMA-doped thin films, which is enhanced significantly in the neat film. This observation can further be correlated to the efficient triplet migration due to long-range molecular ordering, facilitating the efficient annihilation of triplets. Thus, triplet harvesting through TADF and TTA was observed in these donor-substituted phthalimide derivatives. The results presented here, therefore, is proof of concept for exploiting two potentially different mechanisms from a simple phthalimide core by judicious donor substitution. We envisage that our present architecture can

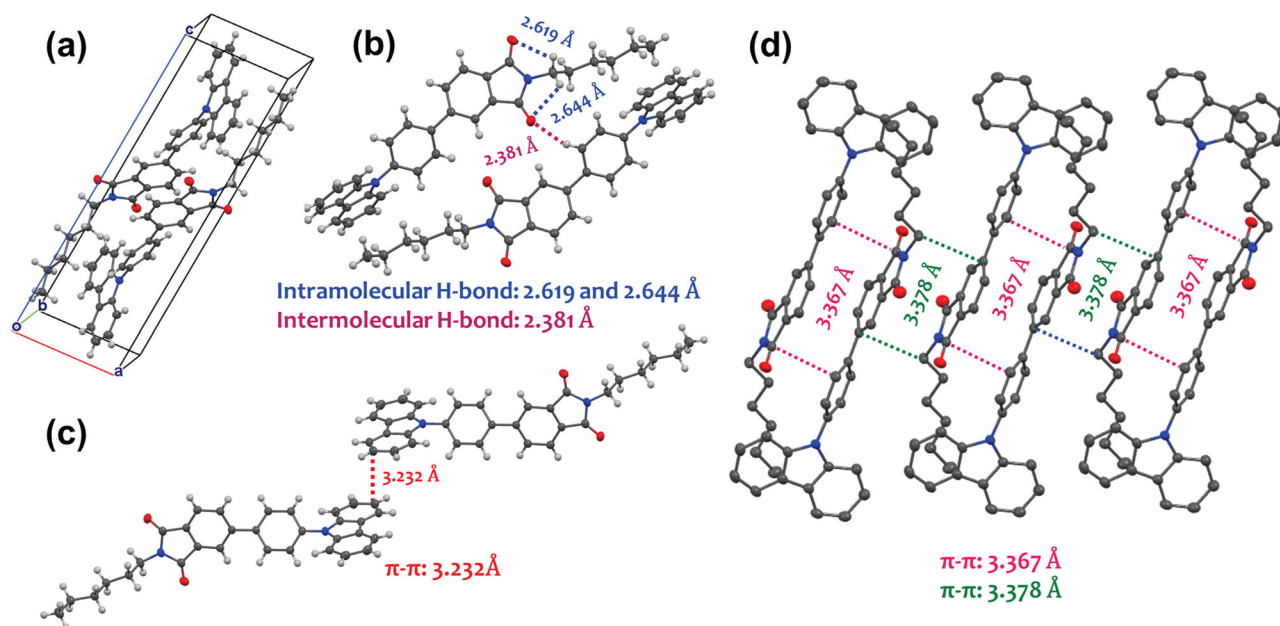


Fig. 7 | Molecular packing and crystal structure analysis of Pth-IPCz. **a** Unit cell, **(b)** intramolecular and intermolecular C–H...O interactions, **(c)** π – π interactions between two units of Pth-IPCz crystal. **d** Slipped stacked arrangement showing

extended stacking with various π – π distances in Pth-IPCz crystal (H atoms are omitted for clarity).

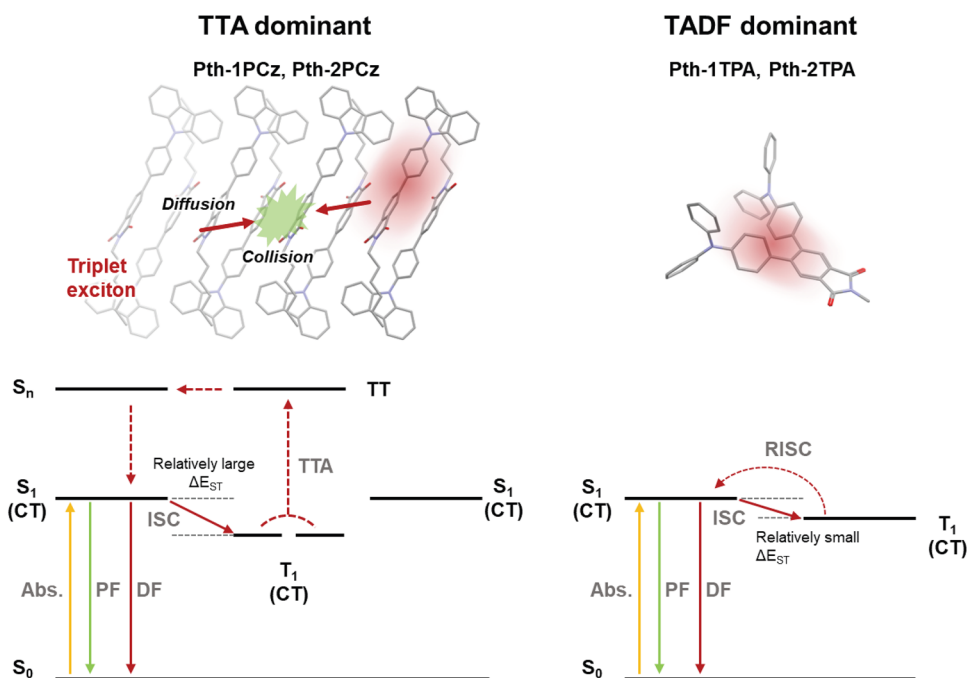


Fig. 8 | Schematic illustration of different delayed fluorescence processes. Proposed TTA-DF and TADF mechanisms in the donor-substituted phthalimide derivatives.

further be extended to the myriad of delayed fluorescence emitters by suitable molecular engineering.

Methods

General methods

All reagents were obtained from commercial sources and used without further purification, and solvents were used as received except specifically mentioned. ^1H and ^{13}C NMR spectra were recorded on a BRUKER AVANCE-400 Fourier transformation spectrometer with 400 and 100 MHz, respectively. CDCl_3 and TMS were used as the solvent and

internal standard, respectively. Matrix-Assisted Laser Desorption Ionization (MALDI) was performed on a Bruker Daltonics Autoflex Speed MALDI TOF System (GT0263G201) spectrometer using trans-2-[3-(4-tert-Butylphenyl)-2-methyl-2-propenylidene]malononitrile (DCTB) as the matrix.

Theoretical methods

The structures of all four phthalimide derivatives were optimized without symmetry constraints using density functional theory (DFT). Absorption spectra were calculated on the ground state geometries,

followed by structure optimization of the first excited states. All calculations were done with Alrich's polarized triple zeta basis sets, excluding f-functions (TVP-f)⁴⁹. Predictions of absorption spectra with the range-separated CAM-B3LYP and B3P86-30% global hybrid functional were compared with experimental absorption spectra in CHCl₃⁵⁰⁻⁵⁴. Solvent effects in the calculations were considered via the polarized continuum model. As usual, CAM-B3LYP predicts absorptions at shorter wavelengths than B3P86-30%⁵⁴. The values for the first absorption peak of Pth-IPCz experimentally at 356 nm, are 313 nm with CAM-B3LYP and 378 nm with B3P86-30%. Similarly, for Pth-ITPA, the experimental value of 405 nm is underestimated as 349 nm with CAM-B3LYP and overestimated as 425 nm with B3P86-30%. Because the B3P86-30% values are closer to the experiment, all further calculations are done with the B3P86-30% functional. Triplet states were calculated at the B3P86-30%/TVP-f level of theory explicitly as triplet ground states to avoid the well-known underestimation of DFT triplet excitation energies. Vertical (vert) triplet energies were obtained as differences between the first excited state (S₁) energy and the ground state triplet (T₁) energy at the ground state (S₀) geometry. Adiabatic (ad) triplet energies were obtained as differences between energies of structure-optimized T₁ and S₁ states. To assess the quality of the triplet energies, CASSCF/NEVPT2 calculations with the same TVP-f basis were done⁵⁵⁻⁵⁷. After many attempts and severe convergence problems, the state-averaged calculations, including 3 singlets and 3 triplets with active spaces of 6 electrons and 6 orbitals, were successful for all four molecules in tetrahydrofuran and in cyclohexane (apart from Pth-2PCz). Therefore, these excited state and triplet energies are done on the S₀ structure and are vertical. The DFT and CASSCF/NEVPT2 values are very similar in cyclohexane, which shows the DFT triplet energies are sound. In THF, CASSCF/NEVPT2 predicts much lower singlet-triplet splitting than DFT. Since state-averaged CASSCF/NEVPT2 calculations do not include state-specific solvation effects, we decided to continue with the ground state triplet energies of the DFT calculations. All calculations are done with the ORCA program version 5.0.3⁵⁸.

Details of photophysical experiments

The UV-visible absorption spectra of the molecules were recorded using a Perkin-Elmer (Lambda 35) spectrometer at room temperature. Steady-state emission spectra were monitored in a Horiba Jobin Yvon Fluorolog-3 fluorometer, and absolute quantum yields were determined in the same instrument using an integrating sphere. Time-resolved fluorescence decay measurements were carried out with the time-correlated single photon counting (TCSPC) method in a Horiba Jobin Yvon Fluorocube instrument with a pulse repetition rate of 10 MHz. Phosphorescence spectra were measured using the phosphorescence mode on a fluorescence spectrometer (Cary Eclipse, Agilent) and the same instrument was used to record some of the time-resolved luminescence measurements using the in-built gated detection mode. Time-gated emission on long timescales was monitored using a nanosecond optical parametric amplifier (EKSPLA, 10 Hz) as the excitation source and a spectrograph (Acton SpectraPro 300i) coupled with a gated intensified CCD camera (Princeton Instruments). Gate and delay times were increased logarithmically to achieve reasonable delayed emission intensity relative to the prompt intensity. The development of this data acquisition method, and hence more details, can be found in the paper by Rothe and Monkman⁴⁵. Low temperature measurements were conducted using a cryostat (Oxford Instruments OptistatDN).

Details of PLDMR measurements

Photoluminescence detected magnetic resonance (PLDMR) was performed using a lab-built optical resonator (based on a dielectric ring resonator), which allows for excitation of the sample and collection of photoluminescence in transmission mode). A 365 nm LED (M365L3 Thorlabs) was used for continuous excitation of the sample, with a

power of ~20 mW. The 365 nm excitation residual was removed via a 400 nm long pass filter. The integrated photoluminescence from >400 nm, 400-550 nm (using a 550 nm short pass filter) or 400-450 nm (using a 450 nm short pass filter) was collected by a silicon detector (Hamamatsu S2281) and the response amplified by a transimpedance amplifier (Femto, DLPCA-200). The PLDMR was carried out at X-band (~9.7 GHz) and the microwaves were square-wave modulated at a frequency of 967 Hz. The change in photoluminescence due to microwave absorption was monitored at the microwave modulation frequency using lock-in detection (Stanford Research Systems SR830) as the static magnetic field was swept through resonance. The temperature was controlled using a Lakeshore 332 temperature controller and a laboratory-built helium flow cryostat. The PLDMR was measured at a temperature of 80 K. Simulations were performed using the toolbox EasySpin version 6.0.0-dev.^{59,60}

Data availability

The authors declare that the data supporting the findings of this study are available within the article and its Supplementary Information files. Additional information is available from the authors on request. The X-ray crystallographic coordinates for structure reported in this study (Pth-IPCz and Pth-2PCz) have been deposited at the Cambridge Crystallographic Data Center (CCDC), under deposition numbers 2293745 and 1538231, respectively. These data can be obtained free of charge from the Cambridge Crystallographic Data Center via <https://www.ccdc.cam.ac.uk/structures/>. Source data are provided with this paper.

References

1. Tang, C. W. & VanSlyke, S. A. Organic electroluminescent diodes. *Appl. Phys. Lett.* **51**, 913–915 (1987).
2. Friend, R. H. et al. Electroluminescence in conjugated polymers. *Nature* **397**, 121–128 (1999).
3. Song, J., Lee, H., Jeong, E. G., Choi, K. C. & Yoo, S. Organic light-emitting diodes: pushing toward the limits and beyond. *Adv. Mater.* **32**, 1907539 (2020).
4. Sasikumar, D., John, A. T., Sunny, J. & Hariharan, M. Access to the triplet excited states of organic chromophores. *Chem. Soc. Rev.* **49**, 6122–6140 (2020).
5. Krishnapriya, K. C., Musser, A. J. & Patil, S. Molecular design strategies for efficient intramolecular singlet exciton fission. *ACS Energy Lett.* **4**, 192–202 (2019).
6. Wong, M. Y. & Zysman-Colman, E. Purely organic thermally activated delayed fluorescence materials for organic light-emitting diodes. *Adv. Mater.* **29**, 1605444 (2017).
7. Forrest, S. The path to ubiquitous and low-cost organic electronic appliances on plastic. *Nature* **428**, 911–918 (2004).
8. Adachi, C., Baldo, M. A., Thompson, M. E. & Forrest, S. R. Nearly 100% internal phosphorescence efficiency in an organic light-emitting device. *J. Appl. Phys.* **90**, 5048–5051 (2001).
9. Baldo, M. A. et al. Highly efficient phosphorescent emission from organic electroluminescent devices. *Nature* **395**, 151–154 (1998).
10. Uoyama, H., Goushi, K., Shizu, K., Nomura, H. & Adachi, C. Highly efficient organic light-emitting diodes from delayed fluorescence. *Nature* **492**, 234–238 (2012).
11. Parker, C. A. & Hatchard, C. G. Delayed fluorescence from solutions of anthracene and phenanthrene. *Proc. R. Soc. London A* **269**, 574–584 (1962).
12. Parker, C. A. Sensitized P-type delayed fluorescence. *Proc. R. Soc. Lond. A* **276**, 125–135 (1963).
13. Zhang, Q. et al. Design of efficient thermally activated delayed fluorescence materials for pure blue organic light emitting diodes. *J. Am. Chem. Soc.* **134**, 14706–14709 (2012).
14. Kaji, H. et al. Purely organic electroluminescent material realizing 100% conversion from electricity to light. *Nat. Commun.* **6**, 8476 (2015).

15. Dias, F. B. et al. Triplet harvesting with 100% efficiency by way of thermally activated delayed fluorescence in charge transfer OLED emitters. *Adv. Mater.* **25**, 3707–3714 (2013).
16. Liu, Y., Li, C., Ren, Z., Yan, S. & Bryce, M. R. All-organic thermally activated delayed fluorescence materials for organic light-emitting diodes. *Nat. Rev. Mater.* **3**, 18020 (2018).
17. Noda, H. et al. Critical role of intermediate electronic states for spin-flip processes in charge-transfer-type organic molecules with multiple donors and acceptors. *Nat. Mater.* **18**, 1084 (2019).
18. Zeng, L., Huang, L., Han, J. & Han, G. Enhancing triplet-triplet annihilation upconversion: from molecular design to present applications. *Acc. Chem. Res.* **55**, 2604–2615 (2022).
19. Cheng, Y. Y. et al. Kinetic analysis of photochemical upconversion by triplet-triplet annihilation: beyond any spin statistical limit. *J. Phys. Chem. Lett.* **1**, 1795–1799 (2010).
20. Serevičius, T. et al. Triplet-triplet annihilation in 9,10-diphenylanthracene derivatives: The role of intersystem crossing and exciton diffusion. *J. Phys. Chem. C* **121**, 8515–8524 (2017).
21. Fallon, K. J. et al. Molecular engineering of chromophores to enable triplet-triplet annihilation upconversion. *J. Am. Chem. Soc.* **142**, 19917–19925 (2020).
22. dos Santos, P. L., Dias, F. B. & Monkman, A. P. Investigation of the mechanisms giving rise to TADF in exciplex states. *J. Phys. Chem. C* **120**, 18259–18267 (2016).
23. Suresh, S. M. et al. A Deep blue B,N-doped heptacene emitter that shows both thermally activated delayed fluorescence and delayed fluorescence by triplet-triplet annihilation. *J. Am. Chem. Soc.* **142**, 6588–6599 (2020).
24. Zhang, J. et al. Boosting organic afterglow efficiency via triplet-triplet annihilation and thermally-activated delayed fluorescence. *J. Mater. Chem. C* **10**, 4795–4804 (2022).
25. Kumar, S., Shukla, J., Kumar, Y. & Mukhopadhyay, P. Electron-poor arylenediimides. *Org. Chem. Front.* **5**, 2254–2276 (2018).
26. Niyas, M. A., Ramakrishnan, R., Vijay, V., Sebastian, E. & Hariharan, M. Anomalous halogen interaction assists radial chromophoric assembly. *J. Am. Chem. Soc.* **141**, 4536–4540 (2019).
27. Bansal, D. et al. A Highly contorted push–pull naphthalenediimide dimer and evidence of intramolecular singlet exciton fission. *Chem. Sci.* **13**, 11506–11512 (2022).
28. Debnath, S. et al. A twist in biphthalimide-based chromophores enables thermally activated delayed fluorescence. *Chem. Mater.* **36**, 4607–4615 (2024).
29. Li, M. et al. Aromatic-imide-based thermally activated delayed fluorescence materials for highly efficient organic light-emitting diodes. *Angew. Chem. Int. Ed.* **56**, 8818–8822 (2017).
30. Feng, Q. et al. A 9-fluorenyl substitution strategy for aromatic-imide-based TADF emitters towards efficient and stable sky blue OLEDs with nearly 30% external quantum efficiency. *Mater. Adv.* **2**, 4000–4008 (2021).
31. El-Sayed, M. A. Spin-orbit coupling and the radiationless processes in nitrogen heterocyclics. *J. Chem. Phys.* **38**, 2834–2838 (1963).
32. Qiu, W. et al. Confining donor conformation distributions for efficient thermally activated delayed fluorescence with fast spin-flipping. *Nat. Commun.* **14**, 2564 (2023).
33. Shi, Y. et al. Optimal dihedral angle in twisted donor–acceptor organic emitters for maximized thermally activated delayed fluorescence. *Angew. Chem., Int. Ed.* **61**, e202213463 (2022).
34. Woo, S. J., Kim, Y. H. & Kim, J. J. Dihedral angle distribution of thermally activated delayed fluorescence molecules in solids induces dual phosphorescence from charge-transfer and local triplet states. *Chem. Mater.* **33**, 5618–5630 (2021).
35. Weissenseel, S. et al. Getting the right twist: influence of donor–acceptor dihedral angle on exciton kinetics and singlet–triplet gap in deep blue thermally activated delayed fluorescence emitter. *J. Phys. Chem. C* **123**, 27778–27784 (2019).
36. Debnath, S. et al. Deciphering intramolecular charge transfer in fluoranthene derivatives. *J. Mater. Chem. C* **12**, 9200–9209 (2024).
37. Garain, S. et al. Arylene diimide phosphors: aggregation modulated twin room temperature phosphorescence from pyromellitic diimides. *Angew. Chem., Int. Ed.* **60**, 12323–12327 (2021).
38. Wada, Y., Nakagawa, H., Matsumoto, S., Wakisaka, Y. & Kaji, H. Organic light emitters exhibiting very fast reverse intersystem crossing. *Nat. Photonics* **14**, 643 (2020).
39. Garain, S. et al. Anion– π -induced room temperature phosphorescence from emissive charge-transfer states. *J. Am. Chem. Soc.* **144**, 10854–10861 (2022).
40. Dias, F. B. Kinetics of thermal-assisted delayed fluorescence in blue organic emitters with large singlet-triplet energy gap. *Philos. Trans. R. Soc. A* **373**, 20140447 (2015).
41. Kobayashi, T. et al. Intersystem crossing rate in thermally activated delayed fluorescence emitters. *Phys. Status Solidi A* **217**, 1900616 (2020).
42. Rothe, C., King, S., Dias, F. & Monkman, A. Triplet exciton state and related phenomena in the β -phase of poly(9,9-Dioctyl) fluorene. *Phys. Rev. B: Condens. Matter Mater. Phys.* **70**, 195213 (2004).
43. Hertel, D., Bässler, H., Guentner, R. & Scherf, U. Triplet-triplet annihilation in a poly(fluorene)-derivative. *J. Chem. Phys.* **115**, 10007–10013 (2001).
44. Partee, J. et al. Delayed fluorescence and triplet-triplet annihilation in π -conjugated polymers. *Phys. Rev. Lett.* **82**, 3673–3676 (1999).
45. Rothe, C. & Monkman, A. P. Triplet exciton migration in a conjugated polyfluorene. *Phys. Rev. B* **68**, 075208 (2003).
46. Franca, L. G., Long, Y., Li, C., Danos, A. & Monkman, A. The critical role of $n\pi^*$ states in the photophysics and thermally activated delayed fluorescence of spiro acridine-anthracenone. *J. Phys. Chem. Lett.* **12**, 1490–1500 (2021).
47. Gan, N. et al. Manipulating the stacking of triplet chromophores in the crystal form for ultralong organic phosphorescence. *Angew. Chem. Int. Ed.* **58**, 14140–14145 (2019).
48. Venkatramaiah, N., Kumar, G. D., Chandrasekaran, Y., Ganduri, R. & Patil, S. Efficient blue and yellow organic light-emitting diodes enabled by aggregation-induced emission. *ACS Appl. Mater. Interfaces* **10**, 3838–3847 (2018).
49. Weigend, F. & Ahlrichs, R. Balanced basis sets of split valence, triple zeta valence and quadruple zeta valence quality for H to Rn: design and assessment of accuracy. *Phys. Chem. Chem. Phys.* **7**, 3297–3305 (2005).
50. Yanai, T., Tew, D. P. & Handy, N. C. A new hybrid exchange–correlation functional using the coulomb-attenuating method (CAM-B3LYP). *Chem. Phys. Lett.* **393**, 51–57 (2004).
51. Perdew, J. P. Density-functional approximation for the correlation energy of the inhomogeneous electron gas. *Phys. Rev. B* **33**, 8822–8824 (1986).
52. Becke, A. D. Density-functional thermochemistry. III. the role of exact exchange. *J. Chem. Phys.* **98**, 5648–5652 (1993).
53. Salzner, U., Pickup, P. G., Poirier, R. A. & Lagowski, J. B. Accurate method for obtaining band gaps in conducting polymers using a DFT/hybrid approach. *J. Phys. Chem. A* **102**, 2572–2578 (1998).
54. Salzner, U. & Aydin, A. Improved prediction of properties of p -conjugated oligomers with range-separated hybrid density functionals. *J. Chem. Theory Comput.* **7**, 2568–2583 (2011).
55. Angeli, C., Cimiraaglia, R., Evangelisti, S., Leininger, T. & Malrieu, J. P. Introduction of n -electron valence states for multireference perturbation theory. *J. Chem. Phys.* **114**, 10252–10264 (2001).
56. Angeli, C., Cimiraaglia, R. & Malrieu, J.-P. n -electron valence state perturbation theory: a spinless formulation and an efficient implementation of the strongly contracted and of the partially contracted variants. *J. Chem. Phys.* **117**, 9138–9153 (2002).

57. Angeli, C., Pastore, M. & Cimiraglia, R. New perspectives in multi-reference perturbation theory: the n -electron valence state approach. *Theor Chem Account.* **117**, 743–754 (2007).
58. Neese, F. Software update: The ORCA Program System-Version 5.0. *Wiley Interdiscip. Rev. Comput. Mol. Sci.* **12**, e1606 (2022). No.
59. Stoll, S. & Schweiger, A. EasySpin, A comprehensive software package for spectral simulation and analysis in EPR. *J. Magn. Reson.* **178**, 42–55 (2006).
60. Tait, C. E., Krzyaniak, M. D. & Stoll, S. Computational tools for the simulation and analysis of spin-polarized EPR spectra. *J. Magn. Reson.* **349**, 107410 (2023).

Acknowledgements

S.D. thanks Council of Scientific & Industrial Research (CSIR), India for Senior Research Fellowship. U.S. thanks Bilkent University, Ankara and Prof. Roi Baer, at the Fritz Haber Research Center for Molecular Dynamics, Institute of Chemistry, Hebrew University of Jerusalem for computational resources. P.R., C.R.H., and T.A.S. acknowledge funding support from the ARC Center of Excellence in Exciton Science (CE170100026). C.R.H. is the recipient of an Australian Research Council Future Fellowship (FT210100113), funded by the Australian Government. N.A.P. is deeply grateful to Professor Robert Bittl and Professor Jan Behrends for their continuous support and for the use of EPR and ODMR labs/setup. W.K. acknowledges the National Research Foundation of Korea (NRF) grant funded by the Korean government (MSIT) (RS-2023-00210400). W.K. was also supported by Global - Learning & Academic research institution for Master's PhD students, and Postdocs (LAMP) Program of the NRF grant funded by the Ministry of Education (RS-2024-00442483). S.P. thanks Science and Engineering Research Board for funding the project through the IRHPA grant IPA/2020/000033 and core research grant CRG/2022/004523.

Author contributions

S.P. conceived the project; S.D. synthesized all the molecules under the supervision of S.P.; S.D. performed structural characterization, steady-state optical measurements, temperature-dependent emission and lifetime measurements under the supervision of S.P.; P.R. performed time-resolved gated emission and intensity-dependent emission experiments under the supervision of T.A.S.; C.R.H. helped in analysis and fitting of time-resolved decays; U.S. performed all theoretical calculations. N.A.P. performed PLDMR experiments and analyzed the results; W.K. participated in discussion to propose the mechanistic pathways presented in the manuscript. All authors discussed and

commented on the experiments and results. The manuscript was written through contributions from all authors. S.D. and P.R. contributed equally.

Competing interests

The authors declare no competing interests.

Additional information

Supplementary information The online version contains supplementary material available at <https://doi.org/10.1038/s41467-025-56987-4>.

Correspondence and requests for materials should be addressed to Satish Patil.

Peer review information *Nature Communications* thanks the anonymous reviewers for their contribution to the peer review of this work. A peer review file is available.

Reprints and permissions information is available at <http://www.nature.com/reprints>

Publisher's note Springer Nature remains neutral with regard to jurisdictional claims in published maps and institutional affiliations.

Open Access This article is licensed under a Creative Commons Attribution-NonCommercial-NoDerivatives 4.0 International License, which permits any non-commercial use, sharing, distribution and reproduction in any medium or format, as long as you give appropriate credit to the original author(s) and the source, provide a link to the Creative Commons licence, and indicate if you modified the licensed material. You do not have permission under this licence to share adapted material derived from this article or parts of it. The images or other third party material in this article are included in the article's Creative Commons licence, unless indicated otherwise in a credit line to the material. If material is not included in the article's Creative Commons licence and your intended use is not permitted by statutory regulation or exceeds the permitted use, you will need to obtain permission directly from the copyright holder. To view a copy of this licence, visit <http://creativecommons.org/licenses/by-nc-nd/4.0/>.

© The Author(s) 2025